



AFRL-RX-WP-TP-2012-0393

**CROSS-CORRELATION FOR AUTOMATED STITCHING
OF TWO-DIMENSIONAL MULTI-TILE ELECTRON
BACKSCATTER DIFFRACTION DATA (PREPRINT)**

J.S. Tiley, A.L. Pilchak, P.A. Shade, and D.L. Ballard
Metals Branch
Structural Materials Division

A.R. Shiveley
Universal Technology Corporation

AUGUST 2012
Interim

Approved for public release; distribution unlimited.

See additional restrictions described on inside pages

STINFO COPY

AIR FORCE RESEARCH LABORATORY
MATERIALS AND MANUFACTURING DIRECTORATE
WRIGHT-PATTERSON AIR FORCE BASE, OH 45433-7750
AIR FORCE MATERIEL COMMAND
UNITED STATES AIR FORCE

REPORT DOCUMENTATION PAGE					Form Approved OMB No. 0704-0188	
<p>The public reporting burden for this collection of information is estimated to average 1 hour per response, including the time for reviewing instructions, searching existing data sources, gathering and maintaining the data needed, and completing and reviewing the collection of information. Send comments regarding this burden estimate or any other aspect of this collection of information, including suggestions for reducing this burden, to Department of Defense, Washington Headquarters Services, Directorate for Information Operations and Reports (0704-0188), 1215 Jefferson Davis Highway, Suite 1204, Arlington, VA 22202-4302. Respondents should be aware that notwithstanding any other provision of law, no person shall be subject to any penalty for failing to comply with a collection of information if it does not display a currently valid OMB control number. PLEASE DO NOT RETURN YOUR FORM TO THE ABOVE ADDRESS.</p>						
1. REPORT DATE (DD-MM-YY) August 2012		2. REPORT TYPE Technical Paper		3. DATES COVERED (From - To) 1 July 2012 – 1 August 2012		
4. TITLE AND SUBTITLE CROSS-CORRELATION FOR AUTOMATED STITCHING OF TWO-DIMENSIONAL MULTI-TILE ELECTRON BACKSCATTER DIFFRACTION DATA (PREPRINT)				5a. CONTRACT NUMBER FA8650-08-C-5226		
				5b. GRANT NUMBER		
				5c. PROGRAM ELEMENT NUMBER 62102F		
6. AUTHOR(S) .S. Tiley, A.L. Pilchak, P.A. Shade, and D.L. Ballard (AFRL/RXCM) A.R. Shiveley (Universal Technology Corporation)				5d. PROJECT NUMBER 4347		
				5e. TASK NUMBER		
				5f. WORK UNIT NUMBER X06B		
7. PERFORMING ORGANIZATION NAME(S) AND ADDRESS(ES) University of North Texas Corner of Ave C Chestnut Denton, TX 76203				8. PERFORMING ORGANIZATION REPORT NUMBER AFRL-RX-WP-TP-2012-0393		
9. SPONSORING/MONITORING AGENCY NAME(S) AND ADDRESS(ES) Air Force Research Laboratory Materials and Manufacturing Directorate Wright-Patterson Air Force Base, OH 45433-7750 Air Force Materiel Command United States Air Force				10. SPONSORING/MONITORING AGENCY ACRONYM(S) AFRL/RXCM		
				11. SPONSORING/MONITORING AGENCY REPORT NUMBER(S) AFRL-RX-WP-TP-2012-0393		
12. DISTRIBUTION/AVAILABILITY STATEMENT Approved for public release; distribution unlimited. Preprint to be submitted to Journal of Microscopy.						
13. SUPPLEMENTARY NOTES The U.S. Government is joint author of this work and has the right to use, modify, reproduce, release, perform, display, or disclose the work. PA Case Number and clearance date: 88ABW-2012-2630, 7 May 2012. This document contains color.						
14. ABSTRACT A method for automatically aligning consecutive datasets of large, two-dimensional multi-tile electron backscatter diffraction (EBSD) scans with high accuracy was developed. The method involves first locating grain and phase boundaries within search regions containing overlapping data in adjacent scan tiles, and subsequently using cross-correlation algorithms to determine the relative position of the individual scan tiles which maximizes the fraction of overlapping boundaries. Savitzky-Golay filtering in two dimensions was used to estimate the background, which was then subtracted from the cross-correlation to enhance the peak signal in samples with a high density of interfaces. The technique was demonstrated on datasets with a range of grain boundary densities. The equations were implemented as enhancements to a recently published open source code for automated stitching of multi-tile datasets.						
15. SUBJECT TERMS SEM, EBSD, cross-correlation						
16. SECURITY CLASSIFICATION OF:			17. LIMITATION OF ABSTRACT: SAR	NUMBER OF PAGES 34	19a. NAME OF RESPONSIBLE PERSON (Monitor) Jaimie Tiley 19b. TELEPHONE NUMBER (Include Area Code) N/A	
a. REPORT Unclassified	b. ABSTRACT Unclassified	c. THIS PAGE Unclassified				

Cross-correlation for automated stitching of two-dimensional multi-tile electron backscatter diffraction data

A.L. Pilchak^{1,2,*}, A.R. Shiveley^{1,2}, P.A. Shade^{1,2},
J.S. Tiley¹, and D.L. Ballard¹

¹Air Force Research Laboratory, Materials and Manufacturing Directorate / RXLM,
Wright Patterson Air Force Base, OH 45432

²formerly, Universal Technology Corporation, Dayton, OH 45433

Abstract

A method for automatically aligning consecutive datasets of large, two-dimensional multi-tile electron backscatter diffraction (EBSD) scans with high accuracy was developed. The method involves first locating grain and phase boundaries within search regions containing overlapping data in adjacent scan tiles, and subsequently using cross-correlation algorithms to determine the relative position of the individual scan tiles which maximizes the fraction of overlapping boundaries. Savitzky-Golay filtering in two dimensions was used to estimate the background, which was then subtracted from the cross-correlation to enhance the peak signal in samples with a high density of interfaces. The technique was demonstrated on datasets with a range of grain boundary densities. The equations were implemented as enhancements to a recently published open source code for automated stitching of multi-tile datasets.

I. Introduction

Electron backscatter diffraction is an advanced scanning electron microscope (SEM) based technique for characterizing the local microstructure and crystallography of materials. The technique was commercialized in the early 1990's and has seen widespread adoption in a variety of fields, most notably geology and materials science. Advances in hardware [Schwarzer, 2008, Schwarzer, 2010] and software [EDAX, Inc., 2007; Bruker Nano GmbH, 2010] technology are pushing acquisition speeds in excess of 1 kHz with further improvements on the horizon. Naturally, this leads to the collection of larger datasets, especially when combined with fast,

precise stage movements [Shiveley, 2011]. This creates two new issues that must be overcome: (1) how to best combine the individual datasets, or tiles, and (2) how to best analyze these datasets that contain tens of millions of data points with file sizes that can exceed 1 GB in raw ASCII format. The latter issue is being tackled by commercial vendors who are taking advantage of 64-bit architecture in their latest software versions, which allows access to much larger blocks of memory. The first issue, however, has received considerably less attention. In previous work, an open source code [Pilchak, 2011] was developed to facilitate combination, or stitching, of two-dimensional, multi-tile datasets in a variety of formats allowing for precise, user-defined positioning of the tiles. The software is especially well suited for datasets with coarser step sizes mapping large areas where precise grain morphology is not an absolutely critical attribute of the analysis. The code also produces generally acceptable results on datasets with fine (sub-micrometer) step sizes where grain-level morphology is of interest, but the inaccuracies inherent to screw-driven SEM stages with rotary encoders inevitably lead to subtle variations in the true tile to tile overlap which introduces artifacts into the seams between adjacent tiles. This is most frequently observed when the stage has to travel a long distance to return to the beginning of a new row. In this work, we expand on our prior software and demonstrate procedures for high accuracy, automated combination of EBSD data from adjacent tiles in a multi-tile dataset using the information contained within the individual tiles.

II. Background

Cross-correlation and convolution are widely used for signal and image processing in many scientific disciplines. Because of their similarities, there is often confusion regarding the two processes and so they are introduced with a simple, yet relevant example. Cross-correlation and convolution are both linear and shift-invariant operations, meaning that the same operation is applied at every point in the discrete representation of the image (or signal). Both involve performing an entry-wise multiplication of two-dimensional arrays which result in the creation of a new array. Consider the rectangular image I and the filter G , shown in Figure 1(a) and (b), respectively. These are binary representations of the right most and left most 50 μm and the entire vertical size (188 μm , at 0.5 μm resolution) of two adjacent tiles in a multi-tile dataset of a hot pack rolled and recrystallized nickel-base superalloy. The cross-correlation of these two arrays is defined as:

$$G \circ I(x, y) = \sum_{l=-N}^N \sum_{k=-N}^N G_{kl} I_{(x+k)(y+l)} \quad (1)$$

where k and l represent the row and column indices of pixels in the filter G , (x, y) are the coordinates of the pixels in I and $2N+1$ is the number of elements in G . The results of the cross-correlation of Figure 1(a) and Figure 1(b) is shown in Figure 1(c). Mathematically, convolution differs only in that the filter is mirrored both horizontally and vertically, i.e.

$$G * I(x, y) = \sum_{l=-N}^N \sum_{k=-N}^N G_{kl} I_{(x-k)(y-l)} \quad (2)$$

The mirrored filter is shown in Figure 1(d), and the resulting convolution of Figure 1(a) and (b), or identically, the cross-correlation of Figure 1(a) and (d), is shown in Figure 1(e). The insets in Figure 1(c) and (e) show the location around the highest intensity at a magnification of 300 times. It is obvious that the cross-correlation produces a strong peak intensity above the background noise. The convolution, on the other hand, produces mainly background noise with numerous local maxima around the strongest intensity. This is, of course, because I (the filter) is mirrored and therefore can never be perfectly matched with G , the image, unless it is symmetric. Thus, the signal in the convolution is primarily related to the density of grain boundary points and the uniformity of their distribution whereas cross-correlation is a direct process. The background noise is essentially due to the fact that there are a nonuniform number of pixels that contribute to the solution to the cross-correlation and convolution for a given (x, y) coordinate. Thus, spurious grain boundary noise is maximized at the central position where the search regions are fully overlapped and tends to decrease toward the periphery of the solution. In fact, it was noted that the shape of the background was similar to that of the instantaneous area of the overlapping regions of G and I when each pixel in the cross-correlation or convolution were calculated as evidenced by Figure 1(f).

This simple example demonstrates why cross-correlation is used for pattern recognition, template matching and image registration. Practical applications include automatic alignment of SEM stages during three-dimensional serial sectioning experiments [Groeber, 2006; Uchic, 2006] and for measurement of surface strains [Kammers, 2001; Walley, 2012], a technique commonly referred to as digital image correlation. Convolution, on the other hand, is commonly used to enhance specific features of an image. Uses include reducing noise prior to segmentation and

feature extraction [Simmons, 2009]. In the standard method of indexing EBSD patterns, a ‘butterfly’ convolution filter is used to enhance the peaks in Hough space associated with specific diffracting (hkl) planes [Schwarzer, 1997]. In image processing, edge detection filters are used to enhance grain or phase boundaries prior to segmentation [Simmons, 2009]. In this work, we demonstrate the use of standard cross-correlation algorithms to automatically combine multi-tile EBSD datasets collected with a combination of beam scans and stage movements.

III. Procedure

First, we briefly describe the overall methodology for automated stitching followed by a more detailed treatment of the individual steps. In this work, previously published source code [Pilchak, 2011] was modified to automatically determine the linear shifts necessary to bring each tile of a multi-tile EBSD dataset into registration. In this formulation, the data points in each tile must be collected on a square grid, though the tiles themselves need not have the same dimensions in the X and Y directions. The major structure of the code, that is, the file naming convention, the sequence in which the tiles are opened and the rules for deciding the location of a particular tile (i.e. first tile, remaining tiles in the first row, each first tile of a new row of data, and internal tiles) was unchanged. Additional functions were added as necessary to perform automated stitching as described below.

Each tile was opened sequentially and treated as the current tile. The neighboring tile(s) relevant for determining its placement were also opened. The data points in each tile that belonged to the so-called search region were extracted and the grain and/or phase boundaries within it were identified resulting in binary arrays similar to those shown in Figure 1(a) and (b). A schematic of the various cases encountered during stitching are shown in Figure 2. Depending on which case is encountered, the size and/or orientation of the search region may change. For border tiles, such as those in the first row or column, tile placement depends on only one neighbor. On the other hand, tile placement depends on two neighbors for internal tiles. In this case, the search regions from the two neighboring tiles are stitched using the previously calculated shifts to create an inverted L shaped search region.

Next, cross-correlation was performed on the grain boundary arrays which revealed the position that maximized the number of overlapping grain/phase boundaries. In datasets with a high density of boundaries, a two-dimensional Savitzky-Golay filter was applied to the result of the cross-correlation to provide an estimate of the background. This result was subtracted from the cross-correlation to increase the signal to noise ratio in order to identify the linear shifts necessary to align the tiles. These, in turn, were used to update the (x,y) coordinates for each pixel in the current tile before appending it to the output file. The approach described above was implemented in MATLAB® and used the *OdPf* function set distributed by the Deformation Processes Laboratory at Cornell University [Dawson, 2011] to perform misorientation calculations quickly.

A. Identification of Grain and Phase Boundaries

Grain and phase boundaries were identified using a [2x2] kernel in a fashion similar to standard edge detection in image processing except, instead of comparing grayscale intensity, the misorientation angle between each pixel and its neighbors in the kernel

$$\begin{bmatrix} 0 & 1 \\ 1 & 1 \end{bmatrix} \quad (3)$$

were used to detect the grain boundaries or “edges”. The kernel was implemented as a sliding window operation which involved calculating the misorientation angle between the pixel beneath the 0 and its neighbors identified by 1’s in the kernel. If the scalar misorientation angle in any of the neighboring bins exceeded a user-defined threshold, typically in the range 5° to 10°, the pixel beneath the 0 was assigned a value of 1 thereby identifying that it was adjacent to a grain boundary. Similarly, the integer identifying the phase associated with each point in the kernel was also compared with its neighbors also assigned a 1 if the phases were different. The result of these operations was a binary array in which the pixels adjacent to grain boundaries are equal to 1 and grain interiors are equal to 0. The method for locating grain boundaries is demonstrated in Figure 3.

Calculations of misorientation can be performed efficiently using the quaternion representation of rotations. Unit quaternions are 4-index vectors which have the form $Q = [q_0, \mathbf{q}] = [\cos(\omega/2), \mathbf{n} \sin(\omega/2)]$ where q_0 and \mathbf{q} are the scalar and vector components, respectively, and satisfy the

relationship $Q = [q_0^2 + q_1^2 + q_2^2 + q_3^2]^{1/2}$. Omega (ω) represents the rotation angle while the unit vector \mathbf{n} represents the rotation axis of the crystallite with respect to the sample reference frame (we adopt Nye's convention [Nye, 1985]). The quaternion misorientation in the fundamental zone, which yields the minimum misorientation angle between two quaternions, Q_A and Q_B , can be determined by finding the minimum rotation angle corresponding to the product of the Q_A^{-1} and Q_B^α :

$$\Delta Q = Q_A^{-1} Q_B^\alpha = [q_{0,A} q_{0,B}^\alpha + \mathbf{q}_A \cdot \mathbf{q}_B^\alpha, q_{0,A} \mathbf{q}_B^\alpha - q_{0,B}^\alpha \mathbf{q}_A - \mathbf{q}_A \times \mathbf{q}_B^\alpha] \quad (4)$$

where the superscript α indicates the use of all symmetrically equivalent orientations of Q_B .

B. Cross-correlation of search regions

Once the grain boundaries in the search region have been identified, the next step is to determine the relative position of the arrays that produces the maximum amount of boundary overlap. The basic form of the calculation is similar for the three types of tiles, namely, those in the first row of data, the first column of data and internal tiles having neighbors both above and to the left. The code was originally developed with the cross-correlation process being performed in the spatial domain before ultimately converting to frequency domain calculations for significantly reduced computational costs.

While the search region arrays containing the grain boundaries are discrete functions, it is still possible to take advantage of the convolution theorem [Bracewell, 1999] which states that the Fourier transform, F , of a convolution (or correlation) of two functions is equivalent to the entry-wise product of the Fourier transforms of the individual functions:

$$F\{\mathbf{L} \circ \mathbf{C}\} = F\{\mathbf{L}\} \cdot (F\{\mathbf{C}\})^* \quad (5)$$

where \mathbf{L} and \mathbf{C} are two-dimensional binary arrays representing the grain boundaries in adjacent search regions in the left and current tiles in the first row of data and the asterisk denotes the complex conjugate. Thus, cross-correlation according to Eq. (1), where \mathbf{L} was fixed and \mathbf{C} is the filter, can be performed quickly to determine the appropriate shifts that align \mathbf{L} and \mathbf{C} which occurs at the location of the peak intensity in the solution to Eq. (5). The offset in pixels (x_o, y_o) can be recovered from the cross-correlation with:

$$x_o = I_{\max} - N_{c,L} \quad (6)$$

$$y_o = k_{\max} - N_{r,L} \quad (7)$$

where (k_{\max}, l_{\max}) is the location of the peak intensity in $F\{\mathbf{L} \circ \mathbf{C}\}$ and $N_{r,L}$ and $N_{c,L}$ are the number of rows and columns in the search region of the left tile. These translate to shifts of

$$x_C = x_L + X_{\text{size}} - x_o X_{\text{step}} \quad (8)$$

$$y_C = y_o Y_{\text{step}} \quad (9)$$

in the spatial domain where (x_C, y_C) are the updated coordinates of the current tile. It is evident that the new x -coordinates depend on those of the prior tile, \mathbf{L} , but the y -coordinates do not for the first row of tiles.

Analogous equations were formulated for the case when the current tile (\mathbf{C}) is the first tile in a new row:

$$F\{\mathbf{U} \circ \mathbf{C}\} = F\{\mathbf{U}\} \cdot (F\{\mathbf{C}\})^* \quad (10)$$

and the offset is recovered and applied with:

$$x_o = l_{\text{peak}} - N_{c,U} \quad (11)$$

$$y_o = k_{\text{peak}} - N_{r,U} \quad (12)$$

$$x_C = x_o X_{\text{step}} \quad (13)$$

$$y_C = y_U + Y_{\text{size}} + y_o Y_{\text{step}} \quad (14)$$

Internal tiles, with neighbors above and to the left, were treated in a different manner. The left and upper tiles are first opened and their boundaries registered in a new array, \mathbf{N} , using the values previously calculated to create an inverted L shape with the remaining part of the array being padded with zeros. The origin of the left tile search region in \mathbf{N} is located at:

$$k = 0 \quad (15)$$

$$l = N_{r,U} - \frac{y_{\text{end},U} - (y_{\text{end},L} - Y_{\text{size}})}{Y_{\text{step}}} \quad (16)$$

while the origin of the search region for the upper tile is at:

$$k = N_{c,L} - \frac{x_{\text{end},L} - (x_{\text{end},U} - X_{\text{size}})}{X_{\text{step}}} \quad (17)$$

$$l = 0 \quad (18)$$

where $(x_{\text{end}}, y_{\text{end}})$ represent the coordinate (in micrometers) of the lower right coordinate of either the left (\mathbf{L}) or upper (\mathbf{U}) tiles. Then, the boundaries in a similar inverted L shaped search region

of the current internal tile were extracted. These two arrays were correlated in the frequency domain,

$$F\{\mathbf{N} \circ \mathbf{C}\} = F\{\mathbf{N}\} \cdot (F\{\mathbf{C}\})^* \quad (19)$$

and the offset was recovered,

$$x_o = l_{\text{peak}} - N_{c,C} \quad (20)$$

$$y_o = k_{\text{peak}} - N_{r,C} \quad (21)$$

and applied in the spatial domain as a function of position with respect to the left tile:

$$x_C = x_L + X_{\text{size}} - x_o X_{\text{step}} \quad (22)$$

$$y_C = y_L + Y_{\text{size}} + y_o Y_{\text{step}} \quad (23)$$

C. Background subtraction

Background noise caused by improperly overlapped grain boundaries was evident throughout the correlations. Generally, the background was sufficiently small that it did not obscure the peak in the cross-correlation, but samples with high densities of boundaries required the background to be estimated and subtracted from the correlation before the correct peak was able to be automatically identified. In early approaches, each point in the correlation was divided by the instantaneous area of the overlapping regions of the search regions at the time that pixel was calculated. While appropriate for some datasets, area normalizing caused creation of some artificial peaks near the edges of the correlation, where the divisor was small, and on others with more dense boundaries. In addition, the shape of the background was dependent on the morphology of the microstructure, and so a more robust, adaptive method was pursued that would estimate the background directly from each solution to the correlation functions.

To this end, Savitzky and Golay's [Savitzky, 1964] smoothing algorithm was used to estimate the background of the two-dimensional cross-correlation function. This filter is known for preserving local maxima and minima that otherwise may be obscured by simple Gaussian, mean and median smoothing filters. The smoothed signal was subtracted from the real signal to produce a background corrected cross-correlation. To obtain the smoothed signal, an odd number of consecutive, equidistant data points (up to 25 in the original formulation, though the equations have been generalized [Madden, 1978]) were fit to a polynomial of the form:

$$p(x) = w_0 + w_1x + w_2x^2 + \dots + w_nx^n = \sum_{m=0}^n w_mx^m \quad (24)$$

where w were smoothing coefficients using a least squares fit. Eq. (24) is typically applied as a sliding window operation in order to smooth an entire dataset. Thus, each pixel becomes the center element of the sliding window and the value in the smoothed dataset is equal to the solution to Eq. (24) evaluated at the same position once the coefficients are known. Savitzky and Golay noted that rather than performing brute force least squares regression, the coefficients can be calculated easily using standard matrix methods,

$$\mathbf{A}\mathbf{w} = \mathbf{c} \quad (25)$$

where \mathbf{w} is a column vector of the coefficients, \mathbf{c} is a column vector of the values neighboring pixels in the kernel (centered on pixel kl) and \mathbf{A} is the design matrix $A_{kl} = k^l$. By multiplying both sides by the transpose of \mathbf{A} ,

$$\mathbf{A}^T\mathbf{A}\mathbf{w} = \mathbf{A}^T\mathbf{c} \quad (26)$$

it can be seen that

$$\mathbf{w} = (\mathbf{A}^T\mathbf{A})^{-1}\mathbf{A}^T\mathbf{c} \quad (27)$$

These equations are solved twice, first row-wise, then column-wise on the already row-smoothed data, in order to produce the two-dimensional background necessary to subtract from the correlations, Eqs. (5), (10) and (19), if necessary.

IV. Results

In this section, we plot solutions to several of the equations presented above for three datasets of varying complexity. The first is a simple, single phase Ti-7Al (wt%) alloy with equiaxed grains of the order of the tile size. The second is a 2 row by 2 column subset of tiles from a polycrystalline nickel-base superalloy prepared via hot pack rolling and recrystallization heat treatment. The third is an $\alpha + \beta$ forged Ti-6Al-4V alloy with large microtextured regions. In the Ti alloy literature, microtextured regions [Sinha, 2007], also called macrozones [Germain, 2007], are known as clusters of equiaxed α grains that have similar c-axis orientation in the hcp lattice but otherwise appear recrystallized / equiaxed in the morphological sense. These are formed by the geometric breakdown of the similarly oriented platelets in α colonies [Bieler, 2002] that were formed during a prior β annealing step in the thermomechanical processing sequence. These datasets were chosen because they have a range of phase and grain boundary densities.

Following each of the detailed analyses, the code is demonstrated on the entire data sets from the Ti-6Al-4V and nickel superalloy samples.

Table 1. EBSD data acquisition parameters for the three demonstration datasets.

Material	Tile size, μm	SEM mag.	Number of tiles (rows, columns)	Step size, μm	Search range, μm
Ti-7Al	115 x 115	800x	30 (5, 6)	0.2	15
Ti-6Al-4V	270 x 270	350x	650 (25, 26)	2	20
Ni-15Al- 5Cr+C,B,Zr	187 x 187	500x	44 (4, 11)	0.5	40

A. Coarse grain, single phase α -titanium

The coarse grained titanium alloy serves as an instructive example because, as evident in Figure 4(a), only one triple point and one grain boundary appear in the search regions for the left and current tiles. Consequently, there is essentially no background noise and the contributions of individual grain boundaries are evident as lines of increased intensity in the solution to Eq. (5), Figure 5(c). These lines have similar slope and orientation to the grain boundary that causes them. As expected, the maximum value of the cross-correlation is located at the intersection of these lines indicating that this is the location of best possible match. There was very little background noise in this coarse grained material, so the maximum in the cross-correlation was sufficient to cover the offset. For thoroughness, however, the Savitzky-Golay estimated background is shown in Figure 5(d) while Figure 5(e) shows the difference between the cross-correlation and the smoothed background. In the cross-correlation, the maximum value is approximately 185 while the adjacent regions are ~ 0 (dark blue regions) and ~ 60 (light blue regions corresponding to grain boundaries) giving a signal to noise ratio of approximately 3:1. In contrast the background corrected peak intensity is ~ 48 while the background noise is ~ 5 , a ratio of nearly 10:1. The results of this cross-correlation are shown in Figure 6. The grain boundaries corresponding to only the overlapping parts of left and current tiles when the cross-correlation is maximized are shown in Figure 6(a) and Figure 6(b), respectively, while the entrywise product

of these arrays appears in Figure 6(c). The inverse pole figure map in Figure 6(d) reveals good matching with no disconnects or seams created on the grain boundaries in the stitched dataset.

B. Polycrystalline nickel-base superalloy

A 2 row by 2 column dataset was combined in this example to show the case for stitching an internal tile. The cross-correlation for the first two tiles appeared as the first example, Figure 1(c). The presence of a slight background, whose shape was similar to the area of overlapping regions at each point in the cross-correlation was noted, but the peak in the correlation was still more intense and therefore easily located. The overlapping parts of the left and current tile arrays at the point where the correlation is maximized, and the entrywise (element-by-element) product of these, are shown with the stitched dataset in Figure 7. Investigation of Figure 7(d) at higher magnifications found no discernible seam between the datasets and no jogs at the grain boundaries. Most importantly, the grains are contiguous across the seam between the tiles and are not separated during the pixel-grouping/grain identification process permitting accurate measurement of grain morphology over large areas with minimal distortion if sufficiently high magnifications are used [Nolze, 2007].

In Figure 8(a), the search regions from the left and upper tiles, which were registered with Eqs. (15) – (18), are shown along with the inverted L shaped search region from the current internal tile. The correlation between these two arrays is shown in Figure 8(b) while the Savitzky-Golay filter (linear fit, window size of 5) is shown in Figure 8(c). Background subtraction, Figure 8(d), essentially flattens the correlation function at this level of resolution, but a single strong intensity of ~1500 compared to the near zero background marks the position of maximum grain boundary overlap. The entrywise product of the search regions corresponding to this peak and a higher magnification image of the peak in the cross-correlation are shown in Figure 9. The white pixels remaining in the entrywise product reveal correspond to the grain boundary pixels that were overlapped at the peak in the cross-correlation function.

The complete dataset is shown in Figure 10(a) while representative 100- μm x 100- μm regions are shown at higher magnification in Figure 10(b) – (d). These regions straddle locations where four tiles meet and have grain boundaries with misorientation angle exceeding 5° highlighted

black. These images also utilize grayscale image quality overlay to highlight the seam between the tiles in Figure 10 (b-e). The first two, b and c, are typical examples of good mating between adjacent tiles where there are no obvious artificial offsets created in the grain boundaries. The arrows in Figure 10(d) call attention to grain morphologies that appear to be incorrect, including a large step in a twin boundary and grain boundary that is precisely parallel and at the very top edge of the lower right tile. However, inspection of the raw data reveals this was in fact the true morphology of the microstructure at this location. Figure 10(e), on the other hand, shows the one example of imperfect mating at the seam that was identified in the polycrystalline dataset. While a small ledge was created at the seam, recall that this was the position that maximized the boundary overlap in the entire search region. The effect of this error on the overall grain boundary and grain size statistics is insignificant.

C. Two-phase $\alpha + \beta$ forged Ti-6Al-4V

The $\alpha + \beta$ forged Ti alloy dataset, Figure 4(c), had the finest grain size and also used the coarsest step size (Table 1). Consequently, there was a higher density of boundaries in the search region and thus the background level exceeded the peak associated with the proper overlap thereby necessitating background subtraction. The search regions for two adjacent tiles, their cross-correlation, the estimated background ($m = 1$, window size = 5) and the background subtracted cross-correlation are shown in Figure 11. Following background subtraction, there is a flat background with an intensity of ~ 20 while the peak is just under 100 giving a signal to noise ratio of $\sim 5:1$. Figure 12 shows the stitched tiles with an image quality overlay to highlight the good matching along the seams between the tiles. Despite the comparatively low signal to noise ratio, the cross-correlation function worked remarkably well to stitch the entire dataset (Figure 13). Due to the large number of grains in this sample, memory errors were encountered when attempting to open the complete stitched dataset and the final map shown in Figure 13 was created by breaking the entire stitched dataset into halves which were able to be opened in the standard commercial packages to create two crystal orientation maps which were merged in standard image processing software.

V. Discussion

Increased data collection rates have necessitated the development of methods for producing large montages of data. In terms of data collection, the generally accepted method now involves collecting a large number of individual tiles that each consist of a standard beam raster scan. This offers two possibilities for analysis. The first is to produce a large amount of data from individual scan tiles and perform statistical analyses of the data in the individual tiles while the second is to produce a single file containing the combined information from all of individual scan tiles. Each method is useful in specific instances, but it is generally desirable to have access to all of the functions in commercial software for characterizing the state of the microstructure, and so the latter method was the impetus for this work.

Execution of the source code from its native form is relatively fast on standard laptops and desktop computers when Eqs. (5), (10) and (19) are solved in the frequency domain. Figure 14 shows a comparison of the processor time required for various operations as a function of the number of elements in the search region for a single stitching operation, i.e. combining only two tiles. The data reveal the significant expense associated with performing correlation in the spatial domain for any reasonable number of elements in the search region. This result supports the choice of applying the convolution theorem, Eq. (5), for performing automated stitching. The times for this operation are all less than 1 second up to ~1000 elements. The most costly function in the code is therefore identifying the pixels adjacent to grain boundaries, though Figure 14 shows that the operation is still executed in a reasonable time.

Prior to converting to the frequency domain method, subset template matching was also investigated as a means for increasing speed. This method was found to be insufficient in terms of accuracy because the peak in the correlation for a subset in one location did not always correspond to the best fit when the entire tile was considered. This is because distortions, uncertainties and assumptions made within the SEM and EBSD acquisition system [Schwarzer, 1995; Nolze, 2007] lead to an uncertainty in the precise position of grain boundaries, particularly near the periphery of scans. Consider Figure 7(c) and Figure 9 which show the entrywise product of the search regions at the location that maximized the cross-correlation function. The boundaries are nominally clear and continuous over the entirety of the individual tiles, but this clarity is only maintained in the central region of the entrywise product of these data (Figure

7(c)). The primary cause of this effect is the trapezium (trapezoidal) distortion that is prevalent at low magnifications where large beam deflection angles must be used to reach the periphery of the scan [Nolze, 2007]. In practice, one usually adjusts the focus to be best at the position $Y_{size}/2$, which also corresponds to the location where the mismatch between two adjacent tiles caused by trapezium distortion is the smallest. Thus, it is tempting to use this as a template centered on $Y_{size}/2$ to perform the cross-correlation. However, it is not trivial to ensure the sample surface is parallel with the x-y plane of the SEM stage and the act of moving the sample may cause the distance between the pole piece and the sample surface to change which changes the y-coordinate in the scan at which the best focus is achieved. Said another way, if the sample surface is not truly at the 70° tilt angle that is expected by the EBSD acquisition system, this introduces yet another distortion [Nolze, 2007]. This distortion, which either foreshortens or lengthens the features of the microstructure depending on the deviation from 70° , will not necessarily result in obvious errors at tile seams as it will be similar for adjacent tiles in a given dataset. However, it is important to recognize that this distortion exists as it may skew measurements of specific features of the microstructure.

There is also reduced beam positioning sensitivity at large deflections from the optic axis which adds uncertainty to the precise location of the beam when a particular data point was collected. Also, because the beam is slightly defocused at the longer or shorter working distance corresponding to the top and bottom of the scan tile, respectively, grain boundaries usually appear more diffuse in image quality or band contrast maps at these locations. Since the present grain boundary formulation operates on a pixel-to-pixel basis, it is easy to see how the aforementioned problems may cause some parts of grain boundaries, or entire boundaries altogether, to not appear in the entry-wise product of the grain boundary arrays corresponding to the maximum intensity in the cross-correlation (Figure 6(c) and Figure 7(c) and Figure 9). In practice, the effect of SEM-induced distortions can be minimized by simply using higher magnifications. Nolz [Nolz, 2007] has shown that a distortion of approximately 2% exists at magnifications of 400x while the 1% threshold is crossed at a magnification of 700x for the instrument used in the investigation. In our SEM (FEI XL30 ESEM), 500x magnification at 25 mm working distance while employing dynamic focus routines was sufficient for multi-tile mapping with minimal distortion observed between the tilt corrected EBSD data and images

taken at zero degree tilt. Imaging of transmission electron microscopy grids at zero tilt and inclined tilt is recommended for quantifying image distortions inherent to each users SEM.

In cross-correlation of images with a distribution of grayscale intensities, it is common practice to scale the intensity values to an interval centered on zero so that overlapping local minima in an image pair contribute toward identifying a correct match, in addition to overlapping local maxima. In the present formulation, this is analogous to setting grain interiors to -1, while still setting boundaries to +1, prior to performing cross-correlation via Eqs. (5), (10) and (19). In preliminary tests, this was found to decrease the strength of the peak signal relative to the background level. More importantly, however, the strength of the peak in the cross-correlation decreased relative to its immediate surroundings and this trend was consistent for most datasets. Ultimately, the same solution was reached after background subtraction. Using the [-1,1] range merely meant that every dataset needed background subtraction leading to overall longer execution times on datasets with a low density of boundaries. Thus, the final version of software uses data on the interval [0,1] and the use of background subtraction is optional. If enabled, the user is required to enter the order of the polynomial and the window size. In most cases, a simple linear fit, $m = 1$ in Eq. (24), over 3-7 data points obtained a sufficient background.

In closing, we recognize that in order to function properly, the present formulation requires EBSD data of relatively high quality. This implies that there are very few improperly indexed pixels. A few guidelines for data collection were developed while writing and testing the code:

- If possible, prepare the sample by electropolishing. This is among the most forgiving ways to polish metallic materials for large-area EBSD evaluation.
- The sample surface should be carefully aligned with the X-Y translation plane of the stage either by precise parallel polishing of the sample, or through the use of an adjustable sample holder.
- The SEM magnification should be sufficiently high that obfuscation of grain boundaries by SEM-induced spatial distortions are minimized.
- The dynamic focus feature should be enabled, if available.
- The size of the overlap region assigned during data collection is a function of the step size, grain size and grain morphology. Users will develop a feel for this for their own

samples to obtain high quality cross-correlations. [Humphreys, 2001], however, has suggested that a minimum of 8-pixels per constituent is necessary to obtain appropriate size statistics and, as a minimum. In the present case, a minimum of about 8 pixels per grain appears to be sufficient to apply these methods.

V. Summary

In summary, we have demonstrated a suitable method for automatically combining multi-tile EBSD datasets with high precision to maintain precise grain morphology in single and two-phase polycrystalline materials. The algorithm simply maximizes the amount of grain, phase and (or) grain and phase boundary overlap between adjacent tiles in EBSD scans and therefore should be applicable to more complex materials as well. Equations were presented for each of the three possible tile positions: first row of data, first column of data and internal tiles. Standard cross-correlation algorithms were successfully applied to recover the linear shifts necessary to translate the EBSD data into proper registration with no artificial seams between the identified boundaries. In datasets with dense boundaries, background estimation was performed using a Savitzky-Golay moving window filter row-wise, then column wise, and this result was subtracted from the cross-correlation. In most cases, a simple linear filter in two directions was sufficient.

Acknowledgments

This work was performed as part of the in-house research activities of the Air Force Research Laboratory's Materials and Manufacturing Directorate. The support and encouragement of laboratory management and helpful discussions with Drs. M. Uchic and M. Groeber (AFRL/RXLM) are gratefully acknowledged. Three of the authors (ALP, ARS, PAS) were supported by Air Force Contract FA8650-07-D-5800 during the time this work was completed. This research was also partially supported by the Institute for Science and Engineering Simulation, Contract FA8650-08-C-5226.

References

Bieler, T.R. & Semiatin, S.L. (2002) The origins of heterogeneous deformation during primary hot working of Ti-6Al-4V. *Int. J. Plast.* vol. 18, 1165–1189.

Bracewell, R., (1999). "Convolution Theorem." *The Fourier Transform and its Applications*, 3rd ed., New York: McGraw-Hill, pp. 108-112, 111.

Bruker Nano GmbH[®]. (2010) *Quantax CrystAlign*. Bruker Nano GmbH, Berlin, Germany.

Dawson, P.R., & Boyce, D., (2011). Polycrystal Simulation Software ODF/PF function set. Cornell University, Ithaca, NY, USA (<http://anisotropy.mae.cornell.edu>).

EDAX[®], Inc. (2007) *Hikari EBSD Camera Installation and Service Manual*. EDAX, Inc.

Groeber, M.A., Haley, B.K., Uchic, M.D., Dimiduk, D.M., & Gosh, S. (2006) 3D reconstruction and characterization of polycrystalline microstructures using a FIB-SEM. *Materials Characterization*, vol. 57, 259-273.

Germain, L., Dey, S.R., Humbert, M., Gey, N., (2007). Determination of parent orientation maps in advanced titanium-based alloys. *Journal of Microscopy*, vol. 227, 284-291.

Humphreys, F.J., (2001). Grain and subgrain characterization by electron backscatter diffraction. *Journal of Materials Science*, vol. 36, 3833-3854.

Kammers, A.D., Daly, S., (2011). Small-scale patterning methods for digital image correlation under scanning electron microscopy. *Measurement Science and Technology*, vol. 22, 125501.

Madden, H.H., (1978). Comments on the Savitzky-Golay Convolution Method for Least-Squares Fit Smoothing and Differentiation of Digital Data, *Analytical Chemistry*, vol. 50, No. 9, 1383-1386.

Nolze, G., (2007). Image distortions in SEM and their influences on EBSD measurements. *Ultramicroscopy*, vol. 107, 172-183.

Nye, J.F., (1985). *Physical Properties of Crystals*, Oxford: Oxford University Press, 276-288.

Pilchak, A.L., Shiveley, A.R., Tiley, J.S., Ballard, D.L., (2011). AnyStitch: a tool for combining electron backscatter diffraction data sets, *Journal of Microscopy*, vol.244, 38-44.

Savitzky, A., Golay, M.J.E., (1964). Smoothing and Differentiation of Data by Simplified Least Squares Procedures, *Analytical Chemistry*, vol. 36, no. 8, 1627–1639.

Schwartz, R.A., (1997). Automated crystal lattice-orientation mapping using a computer-controlled SEM. *Micron*, vol. 28, 249-265.

Schwarzer, R.A., (2008). A fast ACOM/EBSD system. *Archives of Metallurgy and Materials*, vol. 53, 5-10.

Schwarzer, R.A., Hjelen, J., (2010). High-speed orientation microscopy with offline solving sequences of EBSD patterns. *Solid State Phenomena*, vol. 60, 295-300.

- Schwarzer, R.A., Zaefferer, S., Kunze, K., (1995). The characterization of microtexture by orientation mapping. *Advances in X-Ray Analysis*, vol. 38, 547-550.
- Shiveley, A.R., Shade, P.A., Pilchak, A.L., Tiley, J.S., Kerns, R., (2011). A novel method for acquiring large-scale automated scanning electron microscope data. *Journal of Microscopy*, vol. 244, 181-186.
- Simmons, J.P., Chunag, P., Comer, M., Spowart, J.E., Uchic, M.D., & De Graef, M., (2009). Application and further development of advanced image processing algorithms for automated analysis of serial section image data. *Modeling Simul. Mater. Sic. Eng*, vol. 17.
- Sinha, V., Mills, M.J. & Williams, J.C., (2007) Determination of crystallographic orientation of dwell-fatigue fracture factes in Ti-6242 alloy. *J. Mater. Sci.*, **42**, 8334–8341.
- Uchic, M.D., Groeber, M.A., Dimiduk, D.M., & Simmons, J.P., (2006). 3D microstructural characterization of nickel superalloys via serial-sectioning using a dual beam FIB-SEM. *Scripta Materialia* 2006, vol. 55, 23-28.
- Walley, J.L., Wheeler, R., Uchic, M.D., Mills, M.J., (2012). In-situ mechanical testing for characterizing strain localization during deformation at elevated temperatures. *Experimental Mechanics*, vol. 54, pp 405-416.

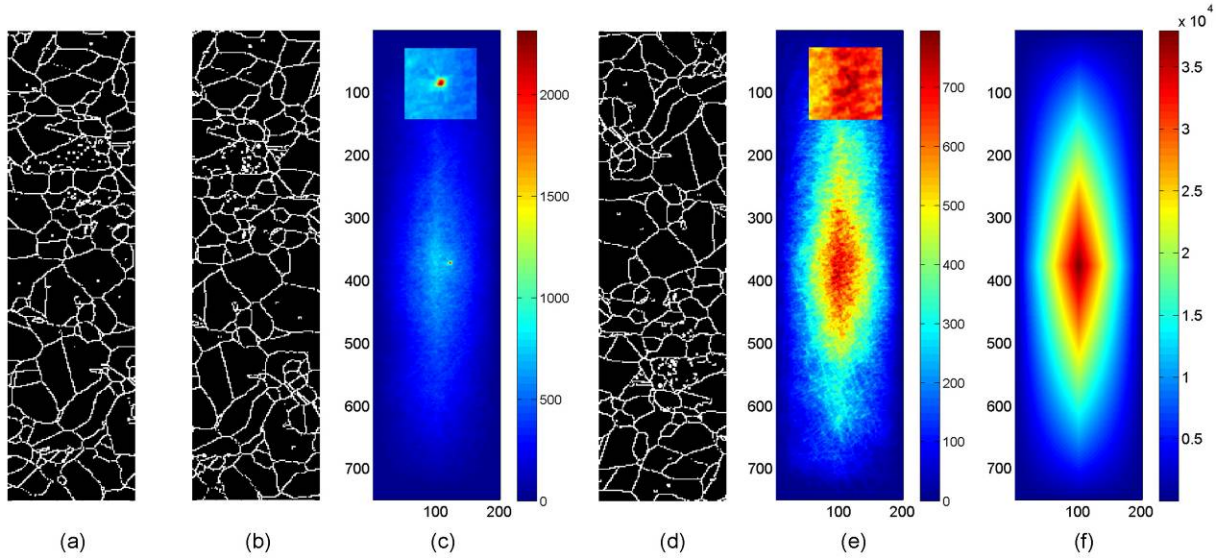


Figure 1. (a) and (b) Binary representation of grain boundaries in the overlapping region of two adjacent tiles of a polycrystalline nickel-base superalloy EBSD dataset. (c) The cross-correlation of (a) and (b). (d) Horizontally and vertically mirrored version of (b). (e) The cross-correlation of (a) and (d), which is equivalent to the *convolution* of (a) and (b). (f) The instantaneous area of the overlapping regions of the tiles at each pixel in the cross-correlation and convolution. The insets in (c) and (e) show the regions around the peak value in each image at a magnification of 300 times.

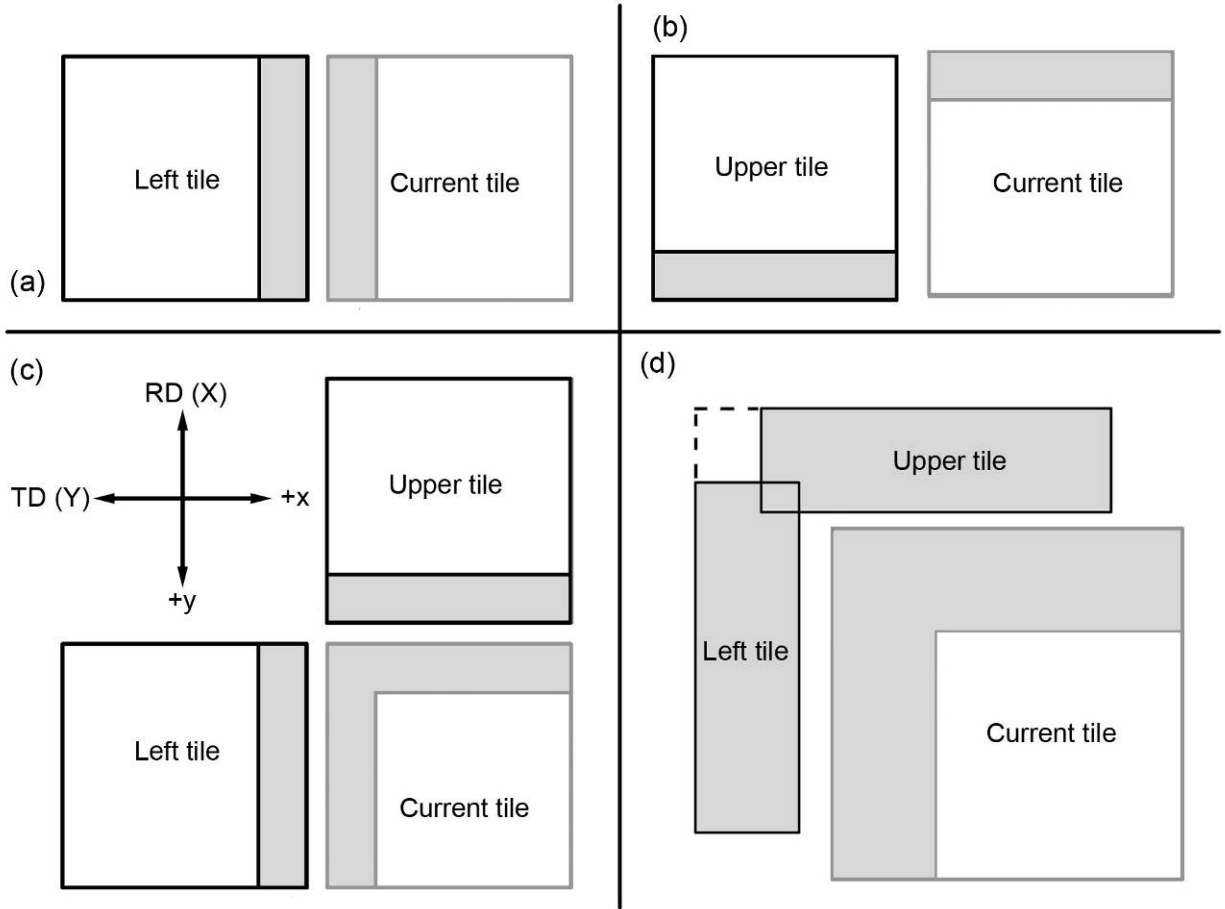


Figure 2. Schematic diagram of the various cases encountered during stitching. (a) First row, (b) first tile of a new row of data, (c) internal tiles and the associated spatial (x,y) and EBSD (X,Y) reference frames. In (d), the left and upper tiles for the internal tile case have been stitched using the previously calculated values prior to performing cross-correlation with the search region of the current tile.

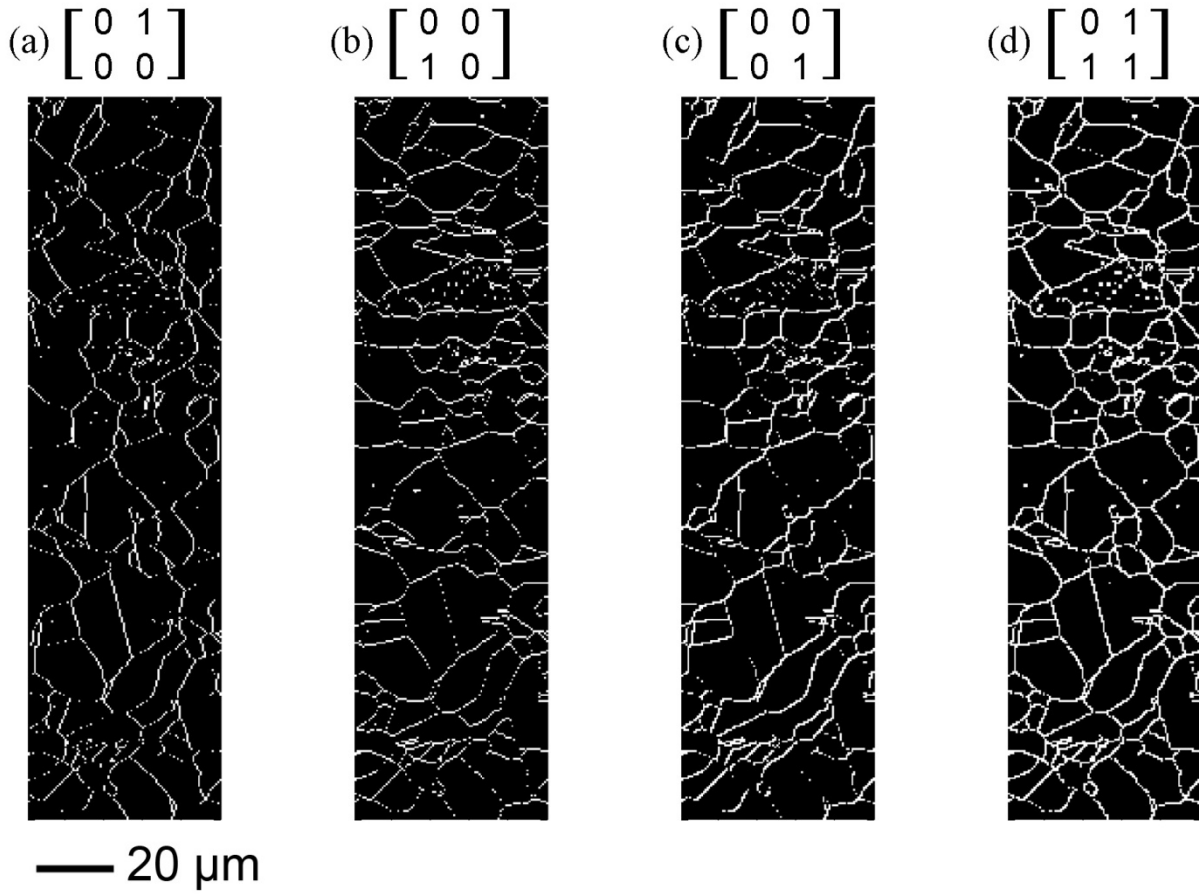


Figure 3. Grain boundary detection using [2x2] kernel. The individual components are shown in (a), (b) and (c) while the combined set appears in (d).

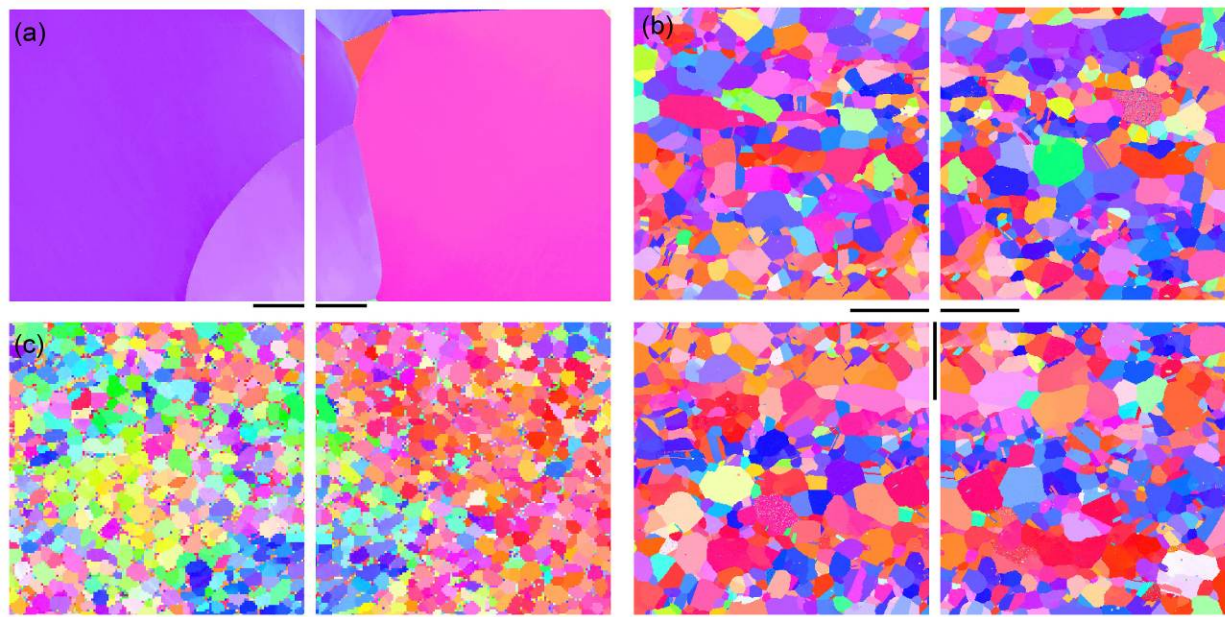


Figure 4. Crystal orientation maps for the first (left) and second (current) tiles of (a) coarse grained α -Titanium, (b) a 2x2 array of a hot pack rolled and recrystallized Ni-Al-Cr superalloy and (c) $\alpha + \beta$ processed Ti-6Al-4V. The scale bars are (a) 20 μm , (b) 30 μm and (c) 50 μm and show the range covered by the search region in each tile.

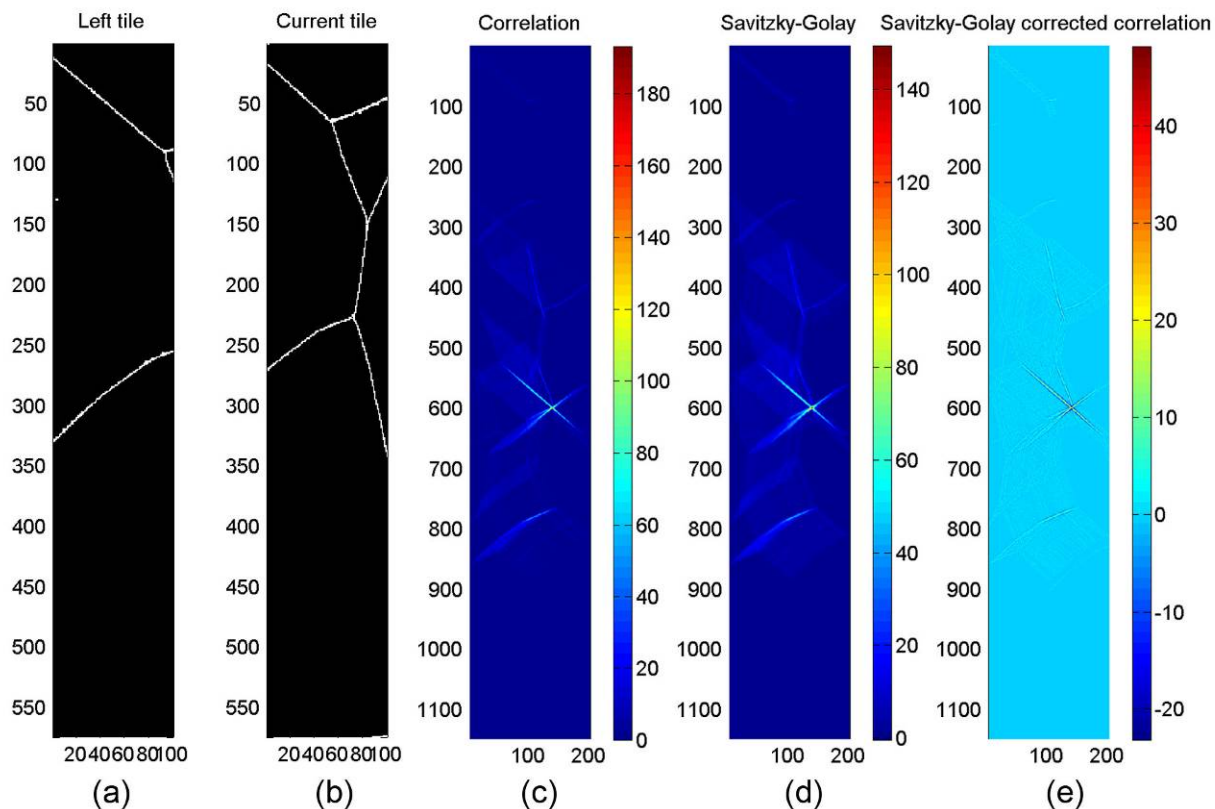


Figure 5. Grain boundaries in the (a) left and (b) current tiles. (c) Cross-correlation of (a) and (b). (d) Savitzky-Golay smoothing of (c) performed with a first order (linear) polynomial and a window size of 3. (e) Difference between (c) and (d).

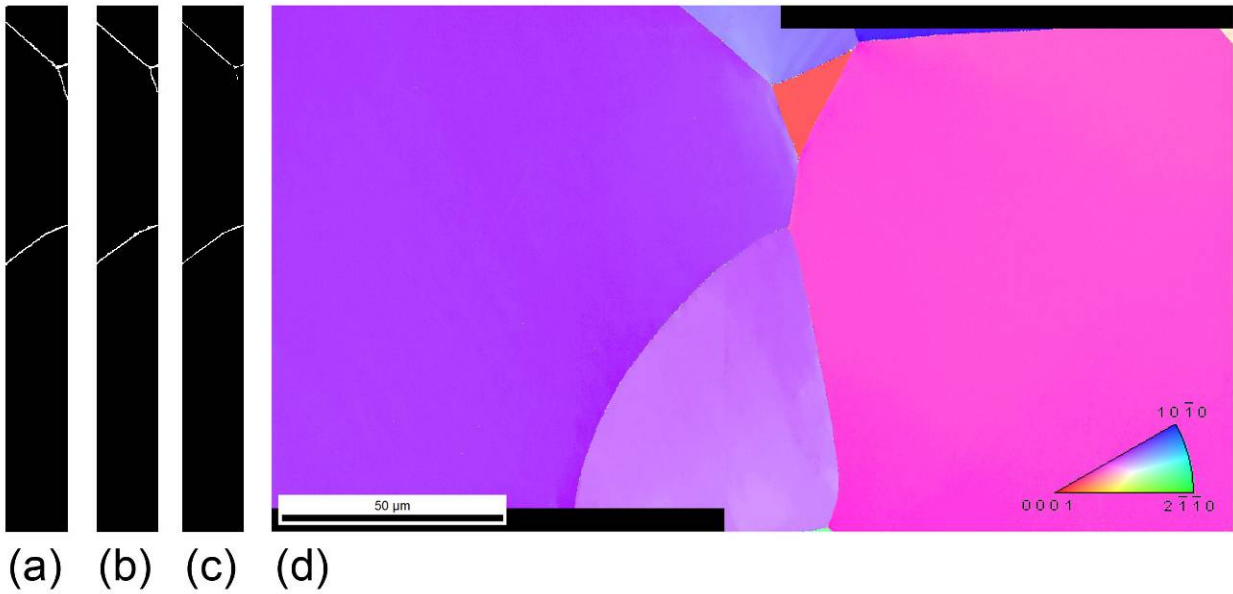


Figure 6. Single phase Ti-7Al (wt%). Binary data showing the grain boundaries in only the overlapping parts of the (a) left and (b) current tiles, and the (c) entry-wise product of (a) and (b) when the cross-correlation function is maximized. (d) Crystal orientation map colored according to the standard triangle for hexagonal materials shown in the lower right corner of the image.

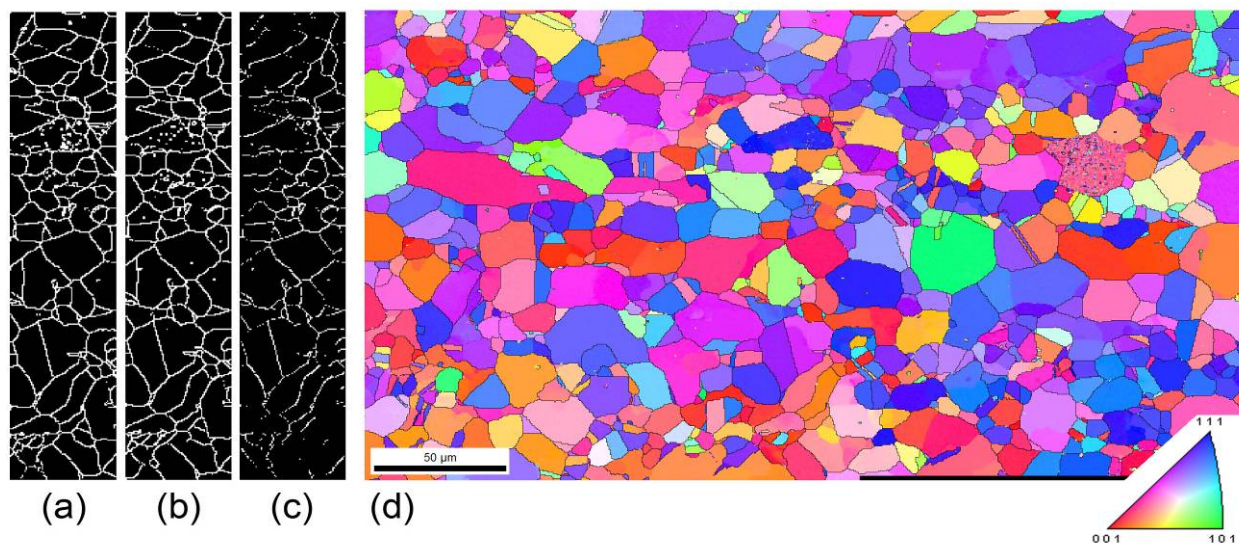


Figure 7. $\gamma + \gamma'$ strengthened Ni-Al-Cr-base superalloy. Binary representation of the grain boundaries in only the overlapping regions of the (a) left tile and (b) current tile, and the (c) entry-wise product of (a) and (b) when the cross-correlation function is maximized. (d) Crystal orientation map colored according to the standard triangle for cubic materials shown in the lower right corner of the image. These two tiles were combined using the correlation shown in Figure 1(c).

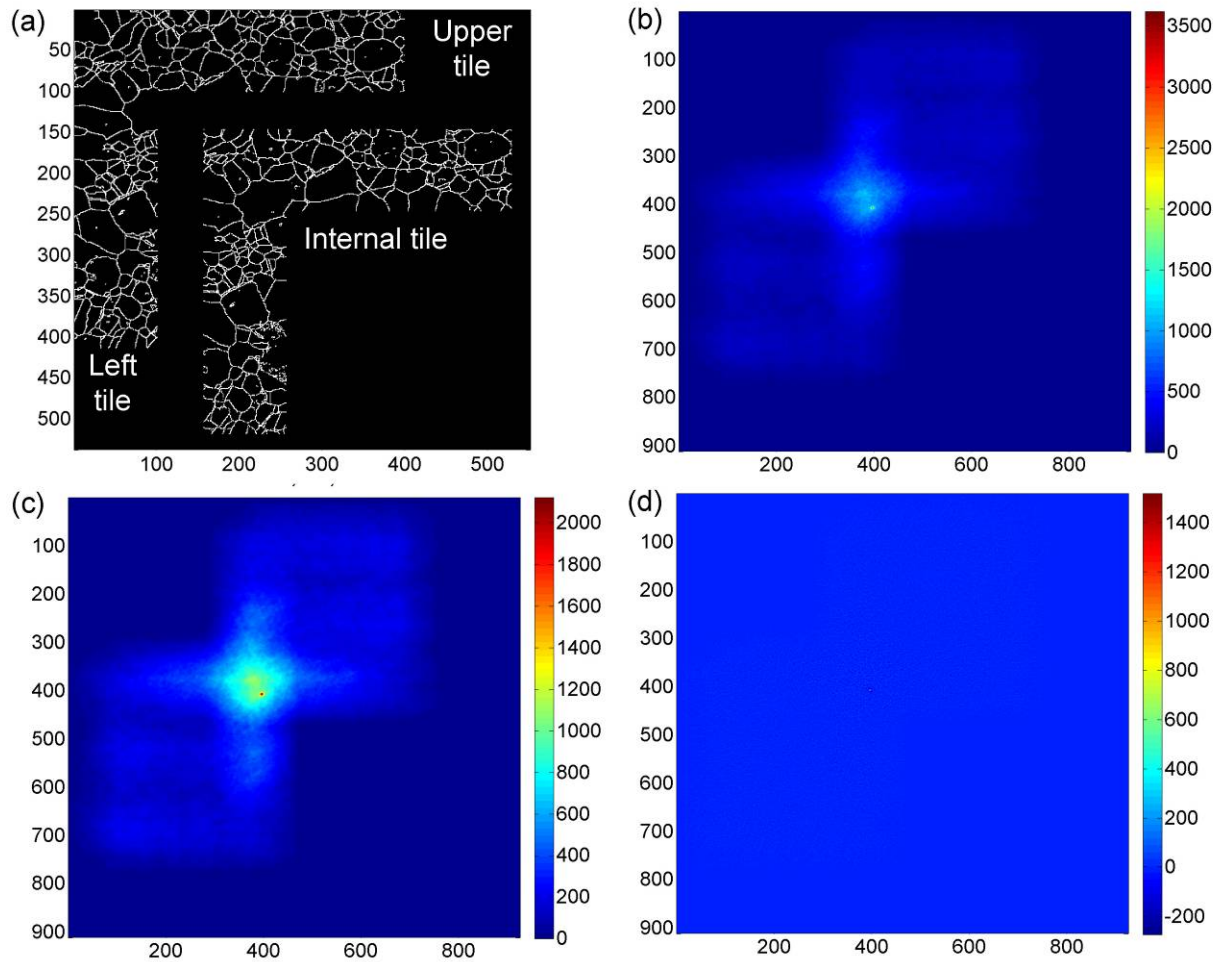


Figure 8. (a) Grain boundaries in the search region of the combined left and upper tiles and the current internal tile in the polycrystalline nickel sample. (b) Correlation of the two regions shown in (a). (c) Savitzky-Golay estimation of the background, linear fit over a window size of 5. All data are shown in pixels where 1 pixel = 0.5 μm . (d) Background corrected cross-correlation. The peak intensity is shown at higher magnification in Figure 9.

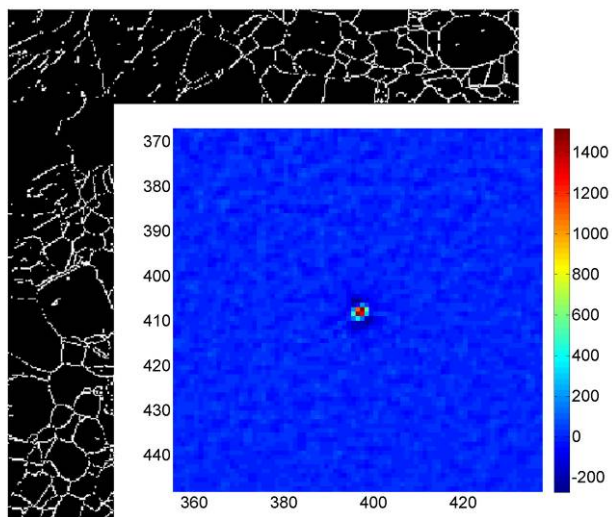


Figure 9. Entry-wise product of the arrays in Figure 8(a) when the background corrected correlation, Figure 8(d), is maximized. The boxed region around the peak in Figure 8(d) is shown at higher magnification.

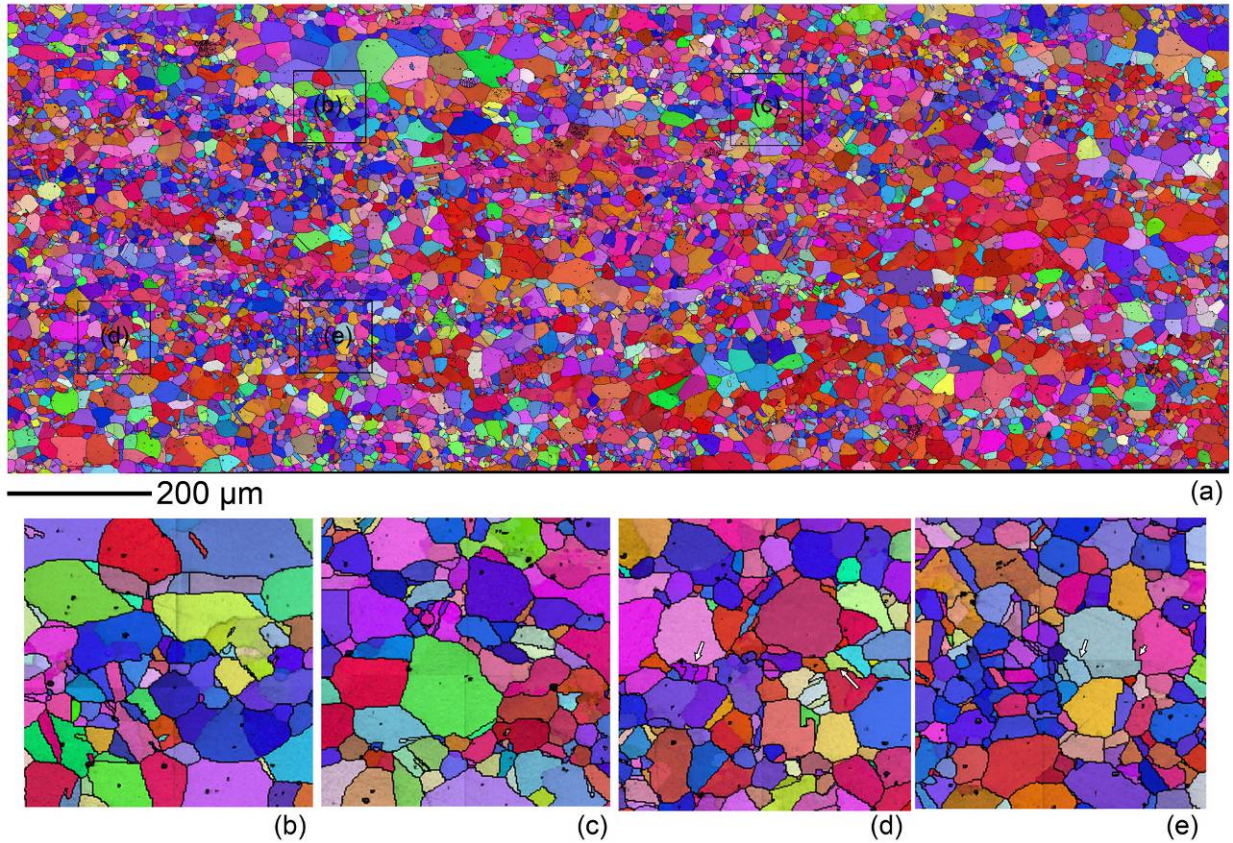


Figure 10. (a) Normal direction inverse pole figure map with image quality overlay and grain boundaries $>5^\circ$ colored black for the 42-tile, polycrystalline Ni superalloy data set. (b), (c) and (d) are 100- μm x 100- μm regions within (a) shown at a magnification of 400x. Faint vertical bands in image quality highlight the seams between adjacent tiles. In (d), some flat segments of grain boundaries parallel to the seam, or large ledges in twins give the impression of an error, but are actually present in the raw data. In (e), the arrows show an example of an artificial step created by the stitching process.

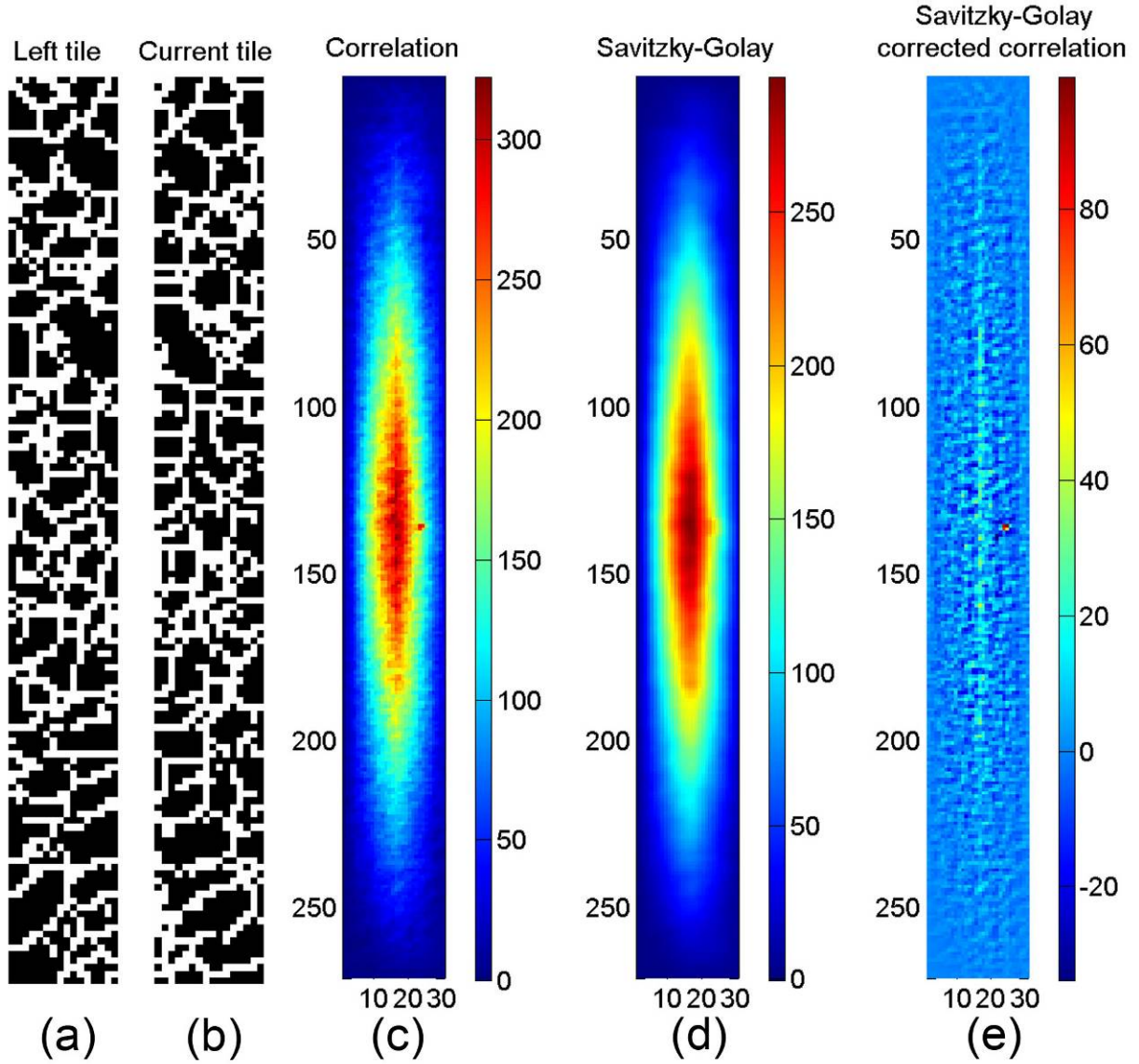


Figure 11. Grain and phase boundaries in the search regions of the (a) left and (b) current tiles of an $\alpha + \beta$ forged Ti-6Al-4V alloy. (c) correlation of (a) and (b). (d) Linear Savitzky-Golay filter ($m = 1$) with a window size of 5. (e) The difference between (c) and (d).



Figure 12. Crystal orientation map (see legend in Figure 6) of $\alpha + \beta$ forged Ti-6Al-4V alloy combined with the correlation shown in Figure 11. The image quality overlay is used to highlight the seam between the tiles which is in approximately the center of the image.

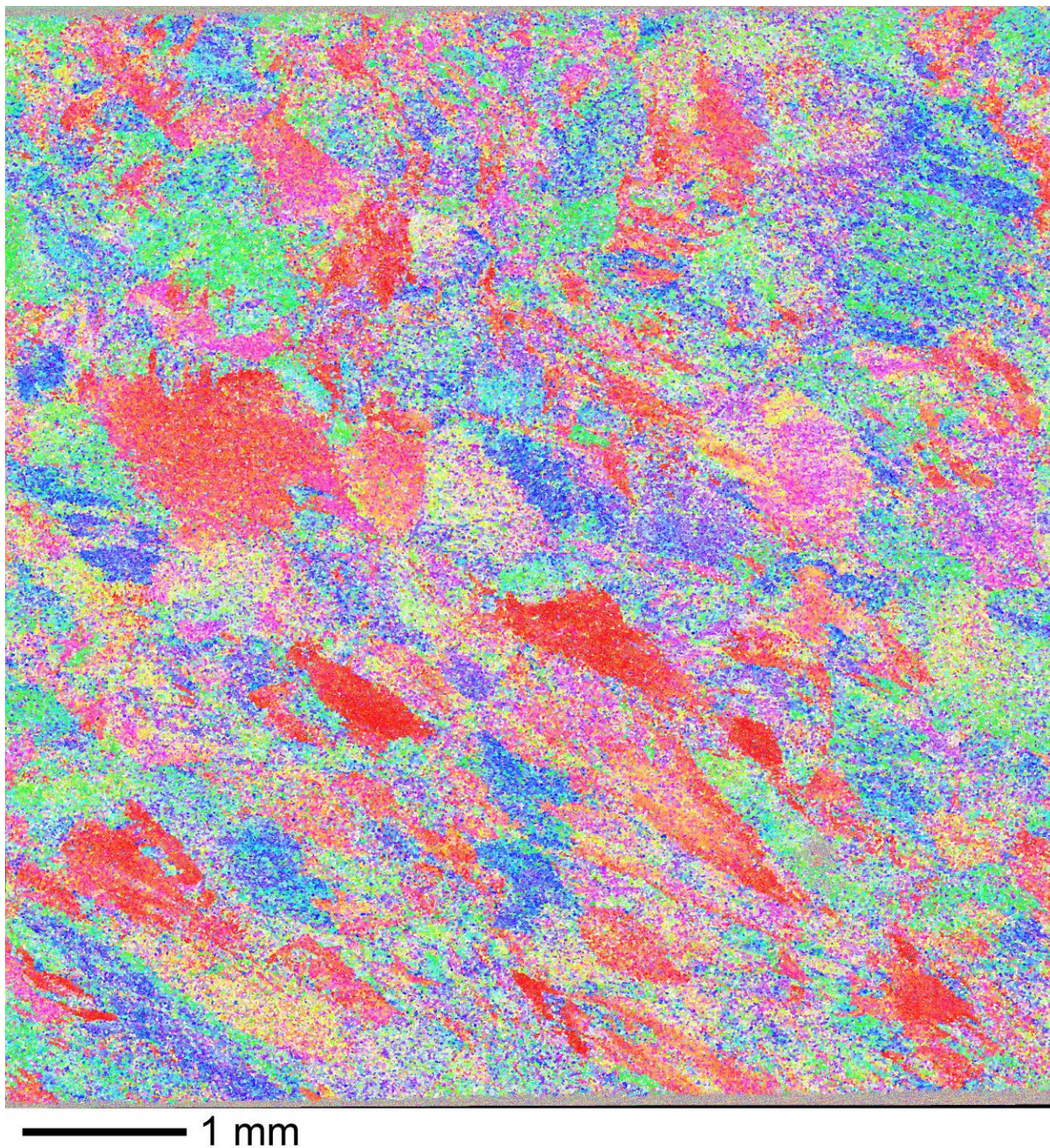


Figure 13. Crystal orientation map (see legend in Figure 6) of the entire dataset for the $\alpha + \beta$ forged Ti-6Al-4V alloy.

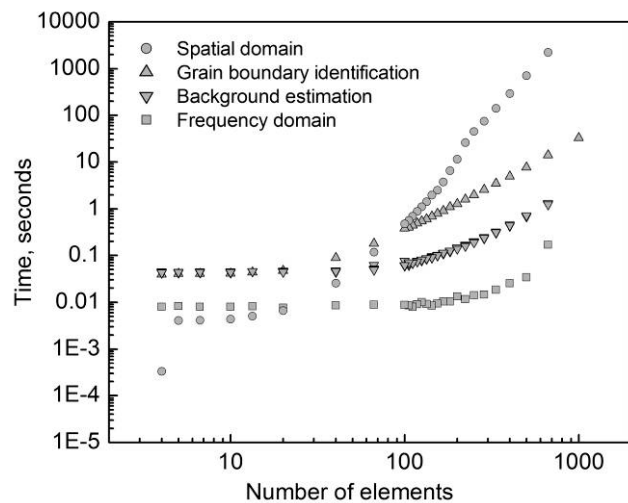


Figure 14. Processor time as a function of number of elements in the search region for the most computationally expensive calculations in the code.